



# Novel extensions to the Fisher copula to model flood spatial dependence over North America

Duy Anh Alexandre, Chiranjib Chaudhuri, and Jasmin Gill-Fortin

Geosapiens Inc., Quebec City, QC, Canada

**Correspondence:** Duy Anh Alexandre (duy-anh.alexandre@geosapiens.ca)

Received: 14 February 2024 – Discussion started: 21 February 2024

Revised: 11 September 2024 – Accepted: 19 September 2024 – Published: 26 November 2024

**Abstract.** Taking into account the spatial dependence of floods is essential for an accurate assessment of fluvial flood risk. We propose novel extensions to the Fisher copula to statistically model the spatial structure of observed historical flood record data across North America. These include the machine-learning-based XGBoost model, exploiting the information contained in 130 catchment-specific covariates to predict discharge Kendall's  $\tau$  coefficients between pairs of gauged–ungauged catchments. A novel conditional simulation strategy is utilized to simulate coherent flooding at all catchments efficiently. After subdividing North America into 14 hydrological regions and 1.8 million catchments, applying our methodology allows us to obtain synthetic flood event sets with spatial dependence, magnitudes, and frequency resembling those of the historical events. The different components of the model are validated using several measures of dependence and extremal dependence to compare the observed and simulated events. The obtained event set is further analyzed and supports the conclusions from a reference paper in flood spatial modeling. We find a nontrivial relationship between the spatial extent of a flood event and its peak magnitude.

events are needed to prevent and mitigate the physical and financial damage caused by flooding.

In fluvial flood models, extreme river discharges are usually derived using observed gauge data. They are commonly used as input to hydraulic models to produce fluvial flood depth maps. Traditionally, flood studies are conducted locally on the scale of a river basin. Many local studies would then be combined to produce flood maps on a national or continental scale. This way of proceeding comes with its limits. Since the methodologies used to assess flood risk can significantly differ from study to study, the aggregation of numerous local studies often lacks coherence (Bates et al., 2023). With current advances in hydrological science, big data, and computing capabilities, flood mapping at a national and continental scale is now possible, taking advantage of the power of more data input (Nearing et al., 2021; Wing et al., 2020; Bates et al., 2021).

Fluvial flooding is inherently a spatial phenomenon: large-scale precipitation and the connectivity of river networks mean that extreme discharge can be present simultaneously at different locations. Modeling widespread flooding is of particular interest for the insurance and reinsurance sectors, since they often operate at a regional and national scale. Some recent studies have shed light on the spatial structure of riverine floods (Brunner et al., 2020; Berghuijs et al., 2019), but this topic is largely understudied. The majority of flood frequency analysis studies do not consider flood spatial dependence, assuming that the same return period flood affects a whole area, an assumption which breaks down if the modeled area is large (Quinn et al., 2019).

Only a few studies have tackled modeling the spatial structure of flood events, usually under stationary conditions (Brunner et al., 2019; Diederer et al., 2019; Keef et al., 2009;

## 1 Introduction

Flooding is one of the most frequent and damaging classes of natural disaster, accounting for 43 % of all major recorded events and affecting nearly 2.5 billion people worldwide during the period 1994–2013 (Centre for Research on the Epidemiology of Disasters, 2015). In hydrology, accurate predictions of the frequency and magnitude of extreme flood

Neal et al., 2013; Quinn et al., 2019). Statistical approaches are commonly used to model multivariate extremes using the theory of max-stable processes (de Haan and Ferreira, 2006; Davison et al., 2012) or copulas (Genest and Favre, 2007). Max-stable processes are parametric models which generalize the univariate extreme value theory to more than one dimension. They have a solid theoretical basis, but because there is no simple parametric form for the target distribution, statistical inference is significantly harder when the number of dimensions is large. Copulas are statistical multivariate structures which separate the marginal distribution of variables from their dependence structure (Genest and Favre, 2007). Copulas have regularly been used to model multivariate extremes in environmental and climate studies: the extreme value copulas (Lee and Joe, 2018; Ribatet and Sedki, 2013), the Archimedean family of copulas (Schulte and Schumann, 2015; Alaya et al., 2018), and spatial vine copulas (Gräler, 2014). Brunner et al. (2019) use the Fisher copula to model co-occurrent extreme floods in a small river basin in Switzerland, with a proposed simple extrapolation to ungauged catchments. Quinn et al. (2019) use the Heffernan and Tawn exceedance model to analyze the spatial dependence between flood peaks for the contiguous United States. They found that extreme river flows were positively correlated, with the correlation decreasing as the distance separating two stations increases. The Heffernan and Tawn conditional exceedance model is gaining popularity in spatial flood modeling, thanks to its basis in extreme value theory, its flexibility, and its easy implementation compared to max-stable processes (Heffernan and Tawn, 2004; Keef et al., 2009). However, compared to copulas, the conditional exceedance model needs the fitting of many regression models and does not present a natural framework to assess spatial dependence at ungauged catchments (Brunner et al., 2019).

In order to create a flood map with complete spatial coverage, methods to model flows in ungauged catchments are needed. Very little past work has tried to model spatially coherent flood including ungauged catchments. Wing et al. (2020) use synthetic discharge simulated by a hydrological model to compensate for lacking observed data and study the spatial structure of floods, although computing rainfall-runoff outputs for every ungauged catchment on a continental scale can represent a high computational burden. Brunner et al. (2019) derived a simple method to extend the Fisher copula model to ungauged catchments, where the pairwise Kendall's  $\tau$  coefficients are regressed against river distance. The authors tested this method on a small subset of 22 stations in a Swiss river basin.

We propose in this study a methodology to model the spatial dependence of a riverine flood on a continental scale based on the Fisher copula model developed in Brunner et al. (2019) and Favre et al. (2018). This model is extended to allow for efficient simulation of floods with spatial coherence in ungauged catchments. The interpolation method in Brunner et al. (2019) is modified to calculate spatially coherent

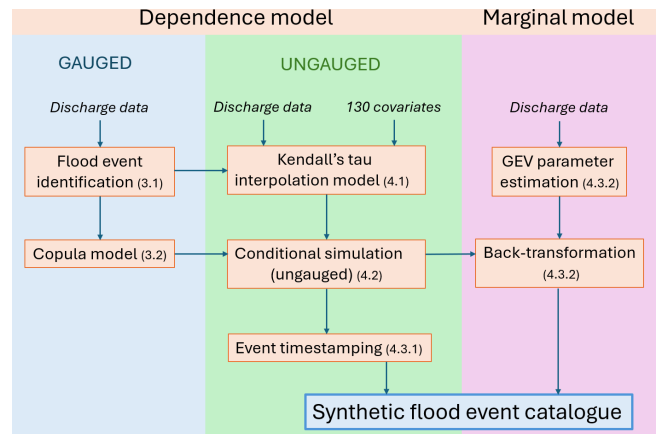


**Figure 1.** Flowchart of the spatial dependence model. The different components are mentioned along with the section number where they are detailed.

ent flows for every catchment using machine learning and a new conditional simulation strategy. Using this probabilistic approach, a synthetic catalog of stochastic discharge events resembling the observed record can be produced, with plausible discharge magnitudes not previously seen. The discharge event set can subsequently be used in hydraulic models to produce a flood depth event set and assess corresponding physical damage and financial losses.

Our methodology includes the following components, which will be addressed in the following sections.

- Event identification from observed records of daily discharge and creation of a regional observed event set are in Sect. 3.1.
- The dependence model for flood events based on the Fisher copula is in Sect. 3.2.
- Interpolation of the Fisher copula model to ungauged catchments is in Sect. 4.1.
- Simulation of a synthetic event set for all catchments, with spatial dependence, is in Sect. 4.2.
- Event time stamping (frequency component) and back transformation with a marginal model for extreme discharge (magnitude component) are in Sect. 4.3.

A summary of the methodology and interrelationships between the different components can be visualized in Fig. 1.

## 2 Data

### 2.1 Daily discharge data

We use daily discharge data from various sources, first starting with data from the Global Runoff Data Centre database

(GRDC; The Global Runoff Data Centre, 2024), an international data center operating under the auspices of the World Meteorological Organization. It consists of 2118 stations high-quality records across North America, with different time periods for each station. This dataset is supplemented by various government sources: USGS National Water data for the USA (U.S. Geological Survey, 2016), Atlas hydroclimatique for Quebec (Ministère de l'Environnement, de la Lutte contre les changements climatiques, de la Faune et des Parcs, 2022), and the HYDAT Database for Canada (Environment Canada, 2013), extracted with the TidyHydat package in R. Because some bad-quality data were found in the latter datasets, a quality control procedure is devised to select only the station records considered reliable. To this end, we compare annual maximum discharges calculated from the daily discharge series with those from a separate annual maxima database. Annual maximum instantaneous peak discharge datasets are extracted directly from USGS National Water data for the USA (U.S. Geological Survey, 2016) and the HYDAT Database for Canada (Environment Canada, 2013). The annual maxima dataset covers 23 283 stations with at least 10 years of quality-checked data. Mean relative error is calculated across concurrent annual maxima for each station. Stations with a mean relative error lower than 10 % calculated over at least 10 years are considered reliable and added to the GRDC data.

To focus on stations with significant discharge, only those with a drainage area higher than 50 km<sup>2</sup> are kept, and any station or year with non-complete daily data is discarded. After this preprocessing, 3385 high-quality stations are used over North America.

## 2.2 Catchment attributes

A large dataset of 130 characteristics for over 1.8 million catchments across North America is used to model floods at ungauged catchments. These include catchment-specific attributes in term of geography (latitude, longitude, altitude), hydrology (average stream slope, drainage length, drainage area, flow direction fraction), climate (solar radiation, wind speed, vapor pressure), and soil properties (silt, sand, clay, and gravel fraction of different soil layers, mean base saturation, and fractional coverage of different land coverage classes). For a detailed description of each variable as well as their sources, the reader can refer to Table S1 in the Supplement.

## 2.3 Catchment delineation

In this section, we describe the methodology employed to generate the river network, delineate catchment boundaries, and establish topological relationships between catchments. The process utilizes a 90 m spatial resolution MERIT-HYDRO digital elevation model (DEM) with an average unit catchment size of 10 km<sup>2</sup> (Yamazaki et al., 2019). The

90 m MERIT-HYDRO DEM forms the basis for deriving the flow direction raster, which is then used to compute the flow accumulation raster. Watershed delineation is performed for each basin, employing a threshold of 10 km<sup>2</sup>. The delineation process involves specific functions within the Arc Hydro Toolbox, following a classic watershed delineation approach, namely StreamDefinition, Stream Segmentation, CatchmentGridDelineation, CatchmentPolygonProcessing, and DrainageLineProcessing.

This methodology is consistently applied across all major watersheds identified within the 90 m MERIT-HYDRO dataset. The primary objective is to optimize watershed sizes to an approximate average of 10 km<sup>2</sup>, contrasting with the typical dataset norm of around 100 km<sup>2</sup>. The integration of functions within the Arc Hydro Toolbox ensures precise attribution of each line to its respective catchment, effectively delineating its connections with downstream features. The scope of this study encompasses the entirety of North America, resulting in a comprehensive dataset comprising 14 246 network groups (NetID) and 1 821 571 delineated catchments (COMID).

Subsequently, each discharge station is mapped to a combination of NetID and COMID, providing a comprehensive association between the stations and their respective catchments within the river network. The decision was made to associate each station with a catchment to simplify the computation of catchment attributes and ensure accurate alignment with the corresponding watercourse. Discrepancies between the actual station position and the reported position are not uncommon. For each station, the disparity between the reported drainage area and the cumulative upstream drainage area of the surrounding basins is calculated. The station is then linked to the watershed with the smallest error. Subsequently, only stations with a difference between the station's drainage area and the catchment area falling below the maximum of either 15 % of the upstream catchment drainage area or 60 % of the catchment unit area (addressing cases of head catchments) were retained (see Fig. S1 in the Supplement for a visual plot of this step).

The catchments are partitioned into 14 hydrologically similar regions across North America, corresponding to level 2 of the HydroBASINS product, which delineates watershed boundaries and provides seamless global coverage of consistently sized and hierarchically nested sub-basins at different scales (Lehner and Grill, 2013). These regions are numbered and named: 1 – Arctic, 2 – Northwest Passage, 3 – Hudson Bay, 4 – Nunavut, 5 – Northwest Territories, 6 – Alaska, 7 – Saint Lawrence, 8 – prairie, 9 – British Columbia, 10 – East Coast, 11 – Midwest, 12 – California, 13 – Mexico, 14 – Caribbean. They are represented in Fig. 2, along with the locations of the preprocessed station data. An example of river network (NetID) and catchment (COMID) delineation is shown in Fig. 3 for region 9, British Columbia.

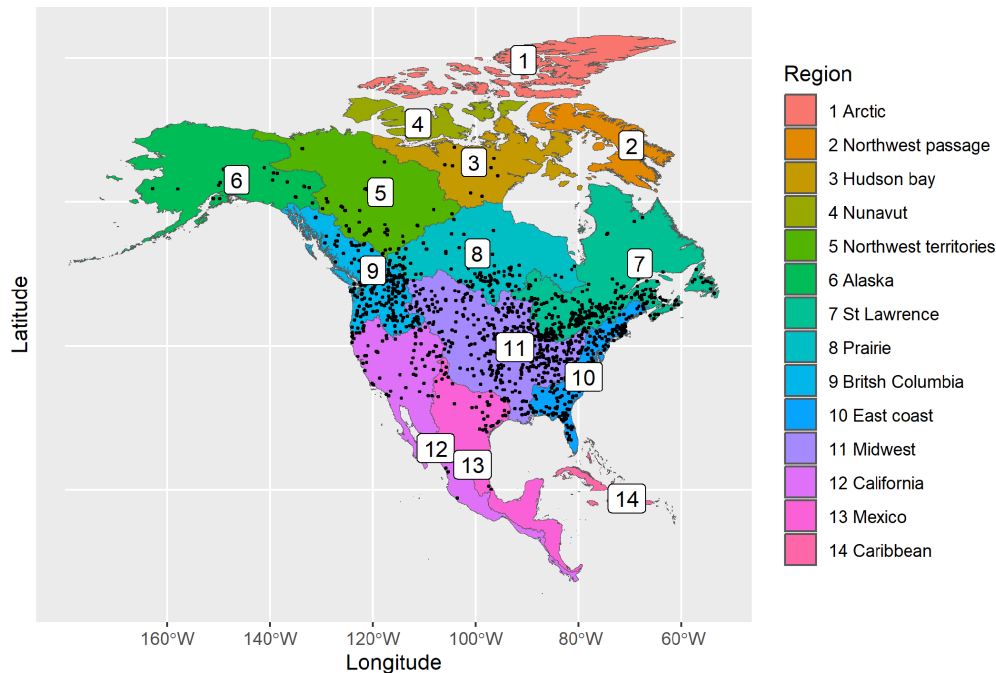


**Figure 2.** The 14 HydroBASINS regions and location of station data after preprocessing (black dots).

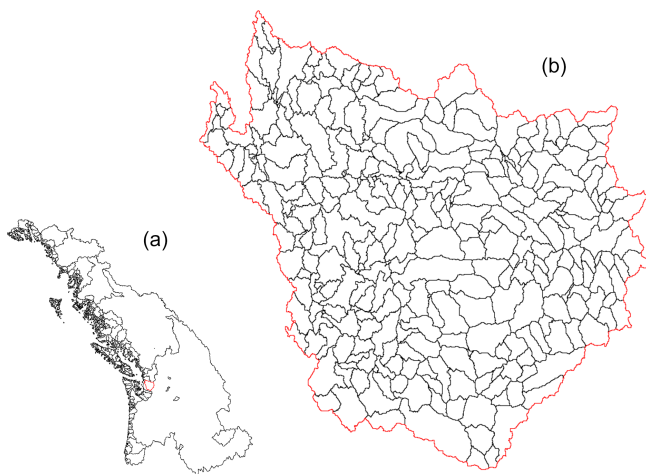


**Figure 3.** Discretization of HydroBASINS region 9 into river networks (a) and of a small river network into catchments (b). The considered network is highlighted with a red contour.

### 3 Dependence model for gauge stations

The subsequent methodology is applied for each HydroBASINS region independently. Catchments within a region can share the same large-scale hydrological behavior, but stations across multiple regions usually exhibit distinct spatial structures. This is supported by recent studies showing that the distance separating catchments experiencing the same floods exhibits regional differences, depending on the nature of flood-generating mechanisms (Berghuijs

et al., 2019; Brunner et al., 2020). Because of station sparsity, we omit analysis of regions 1, 2, 3, 4, 13, and 14 (respectively the Arctic, Northwest Passage, Hudson Bay, Nunavut, Mexico, and the Caribbean). In what follows, the methodology and results are presented for region 9 (British Columbia). Results with regard to regions 7 (Saint Lawrence), 8 (prairie), 10 (East Coast), and 11 (Midwest) can be found in the Supplement (Figs. S4–S10).

### 3.1 Event definition

#### 3.1.1 Synchronous dataset creation

To capture the spatial structure between discharges from multiple stations, observed data have to be available synchronously. For each region, since station data have variable time spans, we choose a sufficiently long common period of observations which maximizes the spatial coverage. To this end, the 30 years (not necessarily continuous) with the highest number of stations are selected as the common time period. Then only stations with complete data coverage for these 30 years and presenting a negligible trend as detected by the Mann–Kendall trend test are retained for analysis. There is a trade-off to be made between the time period length and the spatial coverage, as increasing the time period decreases the number of stations with available data. We consider 30 years to be enough temporal coverage to capture the extreme discharges, and imposing a longer time period would lead to discarding too many stations for some already sparse regions. For British Columbia, 30 years of discharge

record in the period 1975–2013 from 253 stations are used (see Fig. 4a). Gauge density is better in the southern part of the region. The synchronous discharge dataset is then used to define regional events for spatial structure assessment.

### 3.1.2 Event identification

Defining what constitutes a flood event in a continuous series of discharge data is a challenging task implying a number of arbitrary choices. First, local flood events are identified as high peaks at each station using a peak identification algorithm described in Diederer et al. (2019). The algorithm identifies successive alternation of local maxima and minima in the time series, defined as the points where the sign of the increment changes from positive to negative and vice versa. It also includes noise removal and declustering options to remove small perturbations on the one hand and to ensure events are sufficiently separated temporally on the other hand. The threshold for noise removal is taken as  $\delta_y = 0.02 \times \max(dY)$ , where  $dY$  is the series of absolute differences between successive high and low peaks, similar to the work in Diederer et al. (2019). The minimum separating time between two local events is set to 6 d to decluster peaks belonging to the same event and ensure identified events are more or less independent. This is in line with a comprehensive analysis of flood wave travel times by Allen et al. (2018), who show that, globally, flood waves take a median travel time of 6 d to reach their basin terminus. Finally, only peaks exceeding the 0.9th quantile flow for each station are retained, as we are interested in the extreme discharge. Local events are assigned the dates when the maximum peaks occur.

Regional events are identified from the local events using the 1D mean shift clustering algorithm (Comaniciu and Meer, 2002) to group the dates of all local events into clusters. Each cluster corresponds to a time period that defines a regional event. This definition is able to account for the lag time between peak discharges belonging to the same event. As with any clustering algorithm, a choice has to be made with regard to the optimal number of clusters. The algorithm bandwidth is calibrated to obtain between 12 and 24 events per year, on average. This is a trade-off between having enough events to capture the right tail behavior of discharge and avoiding considering small fluctuations around real peaks to be an event. Events containing only one local event are discarded because their natures are not truly regional. A regional event consists of one discharge value for each station using the following rule.

- Stations with a local event happening within a regional event duration are assigned its magnitude. In cases where two or more local events occur within the regional event, the one with the highest magnitude is used.
- For other stations, the maximum discharge magnitude observed during the regional event is assigned. Those

are fill-in values, necessary to assess the flood spatial dependence.

Using a data-based method to obtain regional events allows for variable event durations, identified from the dates of the local peaks. This is a more realistic assumption than the approach adopted in Brunner et al. (2019) and Diederer et al. (2019), where regional events correspond to fixed time windows of 7 and 21 d, respectively.

For British Columbia, 588 regional events are identified (an average of 19.6 events per year), with a mean event duration of 14 d. The mean time interval between two consecutive events is 18.7 d. To describe flood events affecting a large area, the event footprint is often used, defined as the spatial pattern in flood return period for an event (Rougier, 2013). Two examples of observed event footprints are shown in Fig. 4b and c. Stations shown in red are those exceeding the 0.9th quantile threshold. As expected, spatial information is contained in the observed flood events, as high flows tend to occur in spatial clusters.

## 3.2 Fisher copula model

### 3.2.1 Copula theory

The copula theory is based on the representation theorem of Sklar (1959), which states that any multivariate cumulative distribution function  $F_{(X_1, X_2, \dots, X_n)}$  of a set of continuous random variables can be written as

$$F_{(X_1, X_2, \dots, X_n)}(x_1, x_2, \dots, x_n) = P(X_1 \leq x_1, X_2 \leq x_2, \dots, X_n \leq x_n), \quad (1)$$

$$= C(F_1(x_1), F_2(x_2), \dots, F_n(x_n)), \quad (2)$$

where  $F_1, F_2, \dots, F_n$  represent the marginal univariate distributions and  $C$  is termed the copula. One main advantage of the copula approach is that the dependence modeling can proceed independently of the choice of the marginal distributions (Genest and Favre, 2007). The Fisher copula, first introduced in Favre et al. (2018), is defined as the dependence structure of the square of a multivariate Student random vector. It is parameterized by a correlation matrix  $\Sigma$  and a degree of freedom  $\nu$ , corresponding to the same parameters of the Student's  $t$  distribution. When looking at the dependence structure of extreme values, a common measure of interest is the upper tail dependence coefficient, defined for two variables  $X_1$  and  $X_2$  with marginal distributions  $F_1$  and  $F_2$  as

$$\lambda_U = \lim_{u \rightarrow 1} P(X_1 > F_1^{-1}(u) \mid X_2 > F_2^{-1}(u)). \quad (3)$$

This describes the probability that one variable exceeds a high threshold given that the other variable also exceeds a high threshold (approaching the right tail). The Fisher copula allows for modeling in high dimensions, non-vanishing upper tail dependence, and radial asymmetry. It assumes a positive upper tail dependence but asymptotic independence

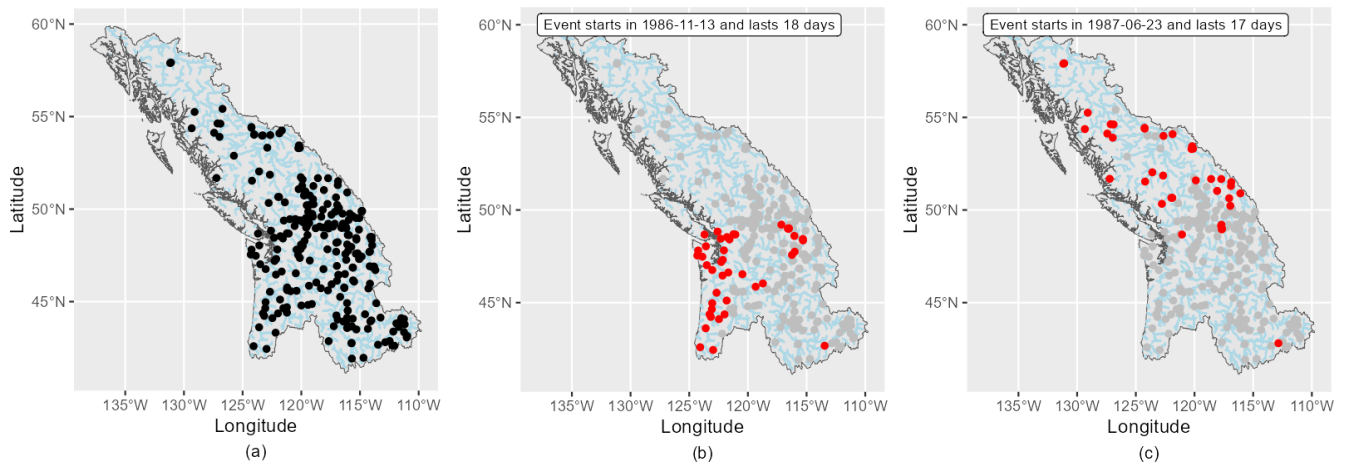


**Figure 4.** Gauge coverage for British Columbia (a) and examples of observed regional event footprints (b, c). Red dots are gauge sites with flows greater than the 0.9th quantile flow during a given event.

(dependence disappears at very large distances between stations). This is a suitable assumption for a riverine flood, as nearby gauges are expected to have correlated discharges, but for distant sites high discharges will almost surely come from independent flood events. When  $\nu \rightarrow +\infty$ , the upper tail dependence vanishes and the Fisher copula approaches the centered chi-square copula.

### 3.2.2 Inference

The Fisher copula parameters are estimated from the regional event set using Kendall's  $\tau$  correlations between pairs of stations. The Kendall's  $\tau$  correlation between two observed random vectors  $\mathbf{x} = (x_1, \dots, x_n)$  and  $\mathbf{y} = (y_1, \dots, y_n)$  is defined as

$$\tau = \frac{2}{n(n-1)} \sum_{i < j} \text{sign}(x_i - x_j) \text{sign}(y_i - y_j), \quad (4)$$

where  $\text{sign}(x) = 1$  if  $x > 0$  and  $-1$  otherwise. It ranges from  $-1$  to  $1$  and is invariant to one-to-one transformations of the variables, making it relatively independent of the marginal distributions. The two-step pseudo-maximum likelihood estimator and Kendall's  $\tau$  inversion method proposed in Favre et al. (2018) are used, exploiting the monotonous relationship between each entry of  $\Sigma$  and the pairwise Kendall's  $\tau$ . Since we work with stations spanning a large spatial scale, some pairs of stations present a negative Kendall's  $\tau$  (15% of the pairs for the region British Columbia). Those values are replaced by zero before Kendall's  $\tau$  inversion, since it requires the  $\tau$  coefficients to be positive. After inversion, the obtained  $\Sigma$  matrix is often non-positive definite. We slightly modify the  $\Sigma$  matrix by replacing negative eigenvalues in the diagonal matrix by a small value, following the idea of Higham (2002), making it positive definite. Using the estimated Fisher copula, a simulated event set of arbitrary length can be generated for all gauge stations.

## 4 Dependence model extended to ungauged catchments

### 4.1 Kendall's $\tau$ interpolation model

In Brunner et al. (2019), the authors developed a method to extend the Fisher copula model to ungauged catchments using a regression model to predict the Kendall's  $\tau$  between all pairs of sites as a function of their river distances. In this way, the correlation matrix  $\Sigma$  was extended to include all catchments, and the new parameters were used to simulate discharge at all catchments. Drawing from this idea, we develop a machine learning model to take advantage of the vast information contained in the 130 catchment-specific characteristics described in Sect. 2.2. Kendall's  $\tau$  between each ungauged catchment and gauge station is predicted with the XGBoost model, as it balances good performance, fast training, and scalability. XGBoost is in the family of boosting models, an ensemble machine learning method which sequentially combines several weak learners (usually shallow decision trees), gradually learning from past mistakes to increase the model performance (Hastie et al., 2009). Grinsztajn et al. (2024) show that among state-of-the-art machine learning models, tree-based models and XGBoost in particular still outperform more complex neural networks on tabular data. XGBoost is extensively used by machine learning practitioners to create state-of-the-art data science solutions, and it has been used successfully for many winning solutions in machine learning competitions.

The absolute differences between pairwise covariates are used as features in the training data. For better performance and to reduce the impact of outliers, the 130 covariates are first-quantile-transformed to normal distributions. Also, because the Kendall's  $\tau$  values lie inside  $[-1, 1]$ , they are logistic-transformed to lie on the real line using the relationship

$$y = \log\left(\frac{(\tau + 1)/2}{1 - (\tau + 1)/2}\right), \quad (5)$$

then used as the targets. Decision trees are used as the base learner, as this is the common choice and allows nonlinearity. The optimal hyperparameters (number of trees, tree depth, learning rate, data and feature subsampling rates, regularizing coefficients) are selected by randomized search 10-fold cross-validation on the training data. The Kendall’s  $\tau$  between pairs of ungauged catchments is not computed, as it is harder to predict accurately and not needed in the conditional simulation strategy explained in Sect. 4.2.

### 4.2 Conditional simulation of events in ungauged catchments

The simulated event set for gauge stations is extended to include all ungauged catchments using the conditional simulation strategy explained below. Let  $(\Sigma_g, \nu)$  be the Fisher copula parameters estimated for the gauged catchments.

First, the Fisher copula can be simulated by transforming simulated values from a Gaussian copula with correlation matrix  $\Sigma_g$ . If

$$Z_1, \dots, Z_n \sim \mathcal{N}_n(\mathbf{0}_n, \Sigma_g), \quad (6)$$

$$C \sim \chi^2(\nu), \quad (7)$$

$$X_i = F_{(1,\nu)}(Y_i) \text{ where } Y_i = \frac{Z_i^2}{C/\nu}, \quad i = 1, \dots, n, \quad (8)$$

where  $n$  is the number of stations,  $\chi^2(\nu)$  is the univariate chi-square distribution with  $\nu$  degrees of freedom, and  $F_{(1,\nu)}$  is the univariate Fisher cumulative distribution function with 1 and  $\nu$  degrees of freedom, then  $(X_1, \dots, X_n)$  follows a Fisher copula and has uniform marginals (Favre et al., 2018). For each simulated event  $(X_1, \dots, X_n)$ , the realized value of  $(Z_1, \dots, Z_n)$  can be stored.

Second, the correlation matrix  $\Sigma_g$  is extended to ungauged catchments using the predicted Kendall’s  $\tau$  from the XGBoost model and Kendall’s  $\tau$  inversion. For each ungauged catchment  $u$ , define an extended correlation matrix  $\Sigma_u$  as

$$\Sigma_u = \left[ \begin{array}{c|c} \Sigma_g & \mathbf{v}_{g,u} \\ \hline \mathbf{v}_{g,u}^\top & 1 \end{array} \right], \quad (9)$$

where  $\mathbf{v}_{g,u}$  represents the correlation entries between catchment  $u$  and the gauge stations, obtained by inverting the predicted Kendall’s  $\tau$  by the XGBoost model described in Sect. 4.1.

Finally, notice that if  $(Z_1, \dots, Z_n, Z_{n+1}) \sim \mathcal{N}_{n+1}(\mathbf{0}_{n+1}, \Sigma_u)$  then  $Z_1, \dots, Z_n \sim \mathcal{N}_n(\mathbf{0}_n, \Sigma_g)$ . We can easily simulate variable  $Z_{n+1}$ , corresponding to catchment  $u$ , conditionally on the realized value  $(Z_1, \dots, Z_n) = (z_1, \dots, z_n)$ , since they are all normal variables. Computation of unobserved discharge  $X_{n+1}$  follows, as described below.

$$\mu_u = \mathbf{v}_{g,u}^\top \Sigma_g^{-1} \mathbf{z} \quad (10)$$

$$\tau_u^2 = 1 - \mathbf{v}_{g,u}^\top \Sigma_g^{-1} \mathbf{v}_{g,u} \quad (11)$$

$$Z_{n+1} | (Z_1 = z_1, \dots, Z_n = z_n) \sim \mathcal{N}(\mu_u, \tau_u^2) \quad (12)$$

$$X_{n+1} = F_{(1,\nu)}(Y_{n+1}) \text{ where } Y_{n+1} = \frac{Z_{n+1}^2}{C/\nu} \quad (13)$$

Here,  $C$ ,  $\nu$ , and  $F_{(1,\nu)}$  are the same as in Eq. (8) and  $\mathbf{z} = (z_1, \dots, z_n)$ . Notice that we use the same value of  $\nu$  previously estimated using gauge stations for reasons discussed in Sect. 7.2. The former procedure is repeated for each ungauged catchment sequentially.

### 4.3 Event set generation

Using the Fisher copula model and proposed extensions to ungauged catchments, a synthetic event set with full spatial coverage can be simulated. Two aspects of the event set need to be addressed at this point, namely the frequency and intensity of simulated events.

#### 4.3.1 Event time stamping

In order to reproduce the temporal distribution of observed events and calculate different annual statistics, simulated events are associated with synthetic dates. Starting from year 0,  $N - 1$  time intervals separating consecutive events are independently sampled using the empirical distribution of separating time between observed events.  $N$  synthetic dates are thus obtained. Each synthetic date is associated with a synthetic event with a given footprint. For historical discharge, events of similar footprint size are usually clustered together in time, representative of seasonal variations between wet and dry periods. To account for the temporal dependence in event footprint size, we simulate a time series of  $N$  event footprints from the empirical distribution, allowing for a positive probability  $p$  that the footprint size is the same for two consecutive events. Comparison of the observed and simulated correlograms is used to calibrate  $p$  in this step. The  $N$  desired event footprint sizes are assigned to the  $N$  synthetic dates. Finally, events in the simulated set are assigned to the synthetic dates by matching their footprints to the desired footprints, with allowance for some small differences.

#### 4.3.2 Back transformation of simulated events

Events simulated using the Fisher copula have uniform margins, by definition. A marginal model is needed to back-transform the simulated values to the discharge scale. Since creating the regional discharge dataset restricts the amount of available data, a marginal model is developed using the discharge annual maxima dataset described in Sect. 2.1, covering more than 23 000 stations. A hierarchical Bayesian model is built to estimate the generalized extreme value (GEV)

distribution parameters for annual maximum discharge in all catchments using the catchment attributes as covariates. Validation of the modeled return period flows against those from government sources can be found in the Supplement for the region British Columbia (Fig. S2). Details regarding this marginal model will be the subject of a separate paper, as the focus of this study is rather on the spatial structure of riverine floods.

Directly back-transforming the simulated values would require a marginal model on the event scale. Instead, the marginal model described above operates on the annual scale. Therefore, before being back-transformed, the simulated values  $q$  are scaled using a scaling factor equal to the (observed) mean number of events per year  $n_y$ :

$$q_{\text{GEV}} = 1 - n_y \times (1 - q). \quad (14)$$

Using the scaling factor  $n_y$  is broadly similar to converting return levels for exceedances calculated with the generalized Pareto distribution to yearly return levels; see chapter 4 of Coles et al. (2001). Then, a discharge level which is exceeded on average once every  $T$  years ( $q_{\text{GEV}} = 1 - 1/T$ ) is exceeded on average once every  $T \times n_y$  events ( $q = 1 - \frac{1}{T \times n_y}$ ).

## 5 Model validation

### 5.1 Fisher copula dependence model

The Fisher copula dependence model is validated by comparing the simulated events (for gauge sites) to the observed events visually and by examining different dependence measures. Figure 5 shows observed and simulated values (on the uniform margin) for a pair of nearby stations (gauges 1 and 2) and a pair of distant stations (gauges 1 and 3) in the region British Columbia. Each point represents a flood event, observed (blue) or simulated (orange). Observed discharges are more correlated between stations 1 and 2 ( $\tau = 0.78$ ) than between stations 1 and 3 ( $\tau = 0.55$ ), reflecting their respective locations, as shown on the left-side map. The Fisher copula is able to suitably reproduce the pairwise correlation of discharge for different dependence strength, especially in the upper tail. This is partly explained by the ability of the Fisher copula to model a wide range of upper tail dependence values (depending on the values of the  $\nu$  and  $\Sigma$  parameters), while the lower tail dependence is always 0; see Favre et al. (2018). Therefore, the Fisher copula might be less well suited for variables correlated in the lower tail, although since the focus is on extreme discharge, this is unlikely to negatively affect the results.

Several dependence measures are also compared for the observed and simulated events. The Kendall's  $\tau$  values between all pairs of stations are compared in Fig. 6a, giving a general picture of the dependence structure. For lower values of  $\tau$  ( $< 0.6$ ), the Fisher copula model tends to slightly

underestimate the correlation, but this is not the case for values higher than 0.6. This is partly due to converting a small number of negative Kendall's  $\tau$  to zero before inversion of Kendall's  $\tau$  values, which can distort the obtained correlation matrix  $\Sigma$ . To assess dependence in the extremes, we look at the F-madogram and the upper tail dependence coefficient (UTD). Usually used to validate max-stable processes, the F-madogram is a pairwise statistic summarizing the spatial dependence structure of the data in the upper tail (Cooley et al., 2006), expressed as a function of the distance between pairs of sites. The F-madograms computed for the simulated events (orange) are compared to the F-madogram of observed events (blue) in Fig. 6b. The dependence pattern is similar for the simulated and observed values. For the UTD, the non-parametric estimator of Schmid and Schmidt (Schmid and Schmidt, 2007) with a cut-off parameter  $p = 0.1$  is used to compare simulated and observed samples in Fig. 6c. The box plot of the UTD differences between simulated and observed events for all pairs of stations is shown in Fig. 6d. Upper tail dependence is very slightly overestimated for the British Columbia region. Still, the comparison shows good agreement, given that this measure is difficult to estimate, especially for a limited observed record length (Serinaldi et al., 2015). Overall, comparison of the different dependence measures shows good agreement between the observed and simulated event set.

### 5.2 Interpolation model to ungauged catchments

The selected XGBoost model is validated using 10-fold cross-validation. This means that 90 % of the training data are used to fit the model and predictions are made on the remaining 10 % of the data in sequence. Figure 7a plots out-of-sample predictions of Kendall's  $\tau$  using the cross-validating models against their true values for each pair of stations. The out-of-sample predicting power of the interpolation model is very satisfying. The Pearson correlation between the out-of-sample predictions and the true values is 0.97.

The XGBoost model outputs are plotted spatially to assess the coherence of predicted Kendall's  $\tau$  with respect to the gauge site. One example of this is shown in Fig. 7b. The spatial dependence pattern is well captured by the model here, as the catchments closest to the gauge station exhibit higher correlation, and correlations decrease as the distance increases. Catchments in the southern part of the region are nearly independent of the gauge site, showing that there is no spatial dependence in their extreme discharges. Geographical distance on its own does not determine the variability of discharge correlation. After fitting the model, feature importance in XGBoost can be assessed by counting the number of times each feature is used in a decision tree. For the region British Columbia, the most relevant catchment characteristics are catchment longitude, dam area, solar radiation, and catchment latitude, followed by wind and some land use indicators (see Fig. S3 in the Supplement). The predicted Kendall's



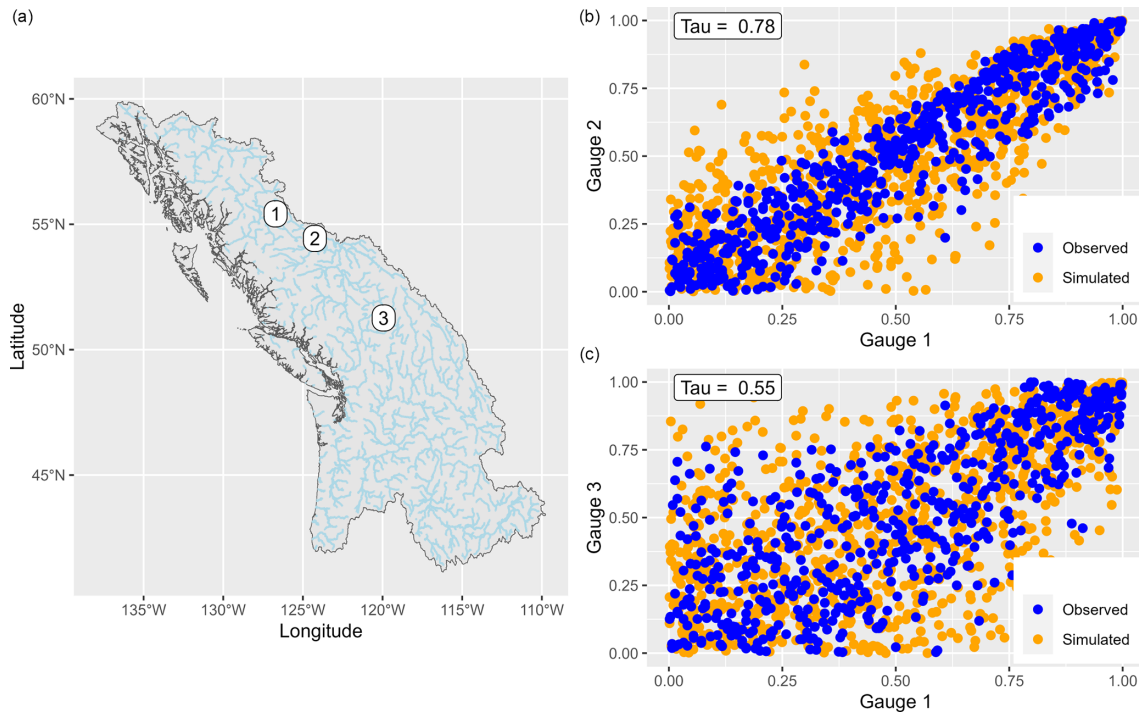


**Figure 5.** Example of pairwise discharge correlation for three stations in the British Columbia region. The observed (blue) and simulated (orange) discharge values are shown for pairs of stations 1–2 and 1–3 (b, c). The geographical locations of the three gauges are also shown (a).

$\tau$  values also provide information on the spatial footprint of events impacting the gauge stations in the data. Some stations measure events with a localized nature (smaller number of predicted high  $\tau$ ), while others are more prone to widespread flood events with a large spatial footprint (not shown).

### 5.3 Simulated event set

To validate the spatial pattern in the simulated event set, it is compared to the observed event set in terms of event footprint size, defined as the number of gauge sites exceeding the 0.9th quantile flow (on the regional event scale). Figure 8 shows the normalized histogram of the footprint size for all observed (red) and simulated events (blue). The observed and simulated events have a similar distribution of footprint size, with high-footprint events being rarer. Half of the events have a footprint size lower than 15 sites (over the 253 gauge sites). The largest event in the observed event set impacts 181 gauge sites. Using stochastic simulation, a high number of widespread events can be generated. Similarly to Quinn et al. (2019), we also compare the mean event footprint size at each gauge site for the observed and simulated events (Fig. 9). The mean is taken over all events impacting a given gauge station with a flow higher than the 0.9th quantile flow. We see that the mean footprint size is reasonably well reproduced in the simulated events, especially for sites with a higher mean event footprint size.

To validate the allocation of events into synthetic years, we calculate for each year (in the observed and simulated event set) the sum of all event footprint sizes and the maximum event size. This is roughly equivalent to computing the annual aggregate loss (AAL) and annual maximum loss (AML), where loss is approximated by the number of gauge sites exceeding the 0.9th quantile flow (Keef et al., 2013). Loss exceedance curves for the annual aggregate and maximum loss are then calculated by empirical estimation and compared for the observed (black dots) and simulated event set (blue line) in Fig. 10. We use 10 000 random samples of a 30-year period taken from the simulated years to calculate the mean and 95 % confidence interval for the simulated loss exceedance curves. This is meant to reproduce the uncertainty range stemming from having a limited record length of 30 years, as is the case with the observed event set. For both aggregate and maximum annual loss, the observed losses lie well inside the uncertainty range calculated with the simulated events. The estimates closely agree for the AAL, while the simulated AML is slightly lower than the observed AML for lower return periods (< 5 years). Overall, the annual loss statistics are well reproduced by the simulated events.

The marginal back transformation is validated by comparing the return period levels calculated from the events and those provided by the marginal model in Sect. 4.3.2, taken as ground truth. This would ensure the validity of the GEV quantiles  $q_{\text{GEV}}$  calculated in Sect. 4.3.2, used to retrieve the

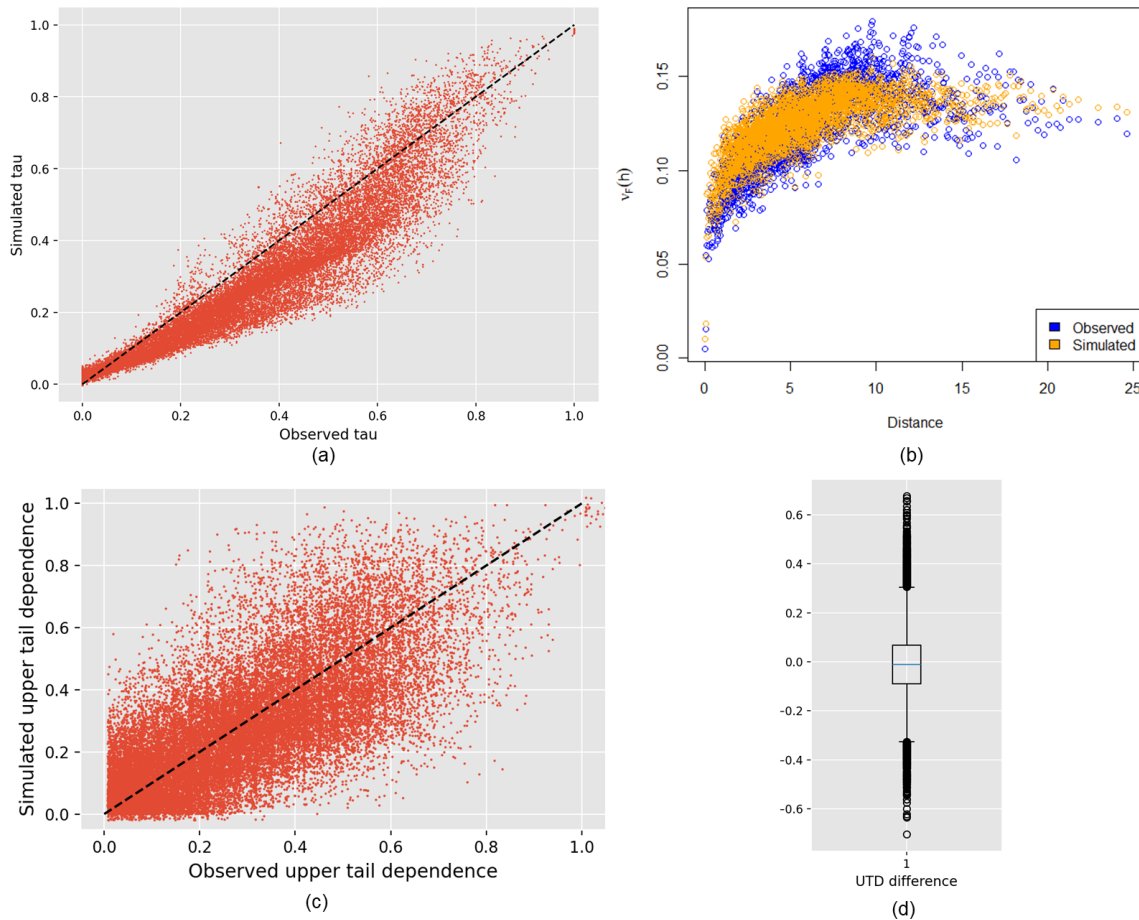


**Figure 6.** Validation of the Fisher copula model is done by comparing different measures for the observed and simulated events: pairwise Kendall's  $\tau$  (a), F-madogram (b), and upper tail dependence (c). The box plot in panel (d) represents the distribution of the differences between simulated and observed UTDs.

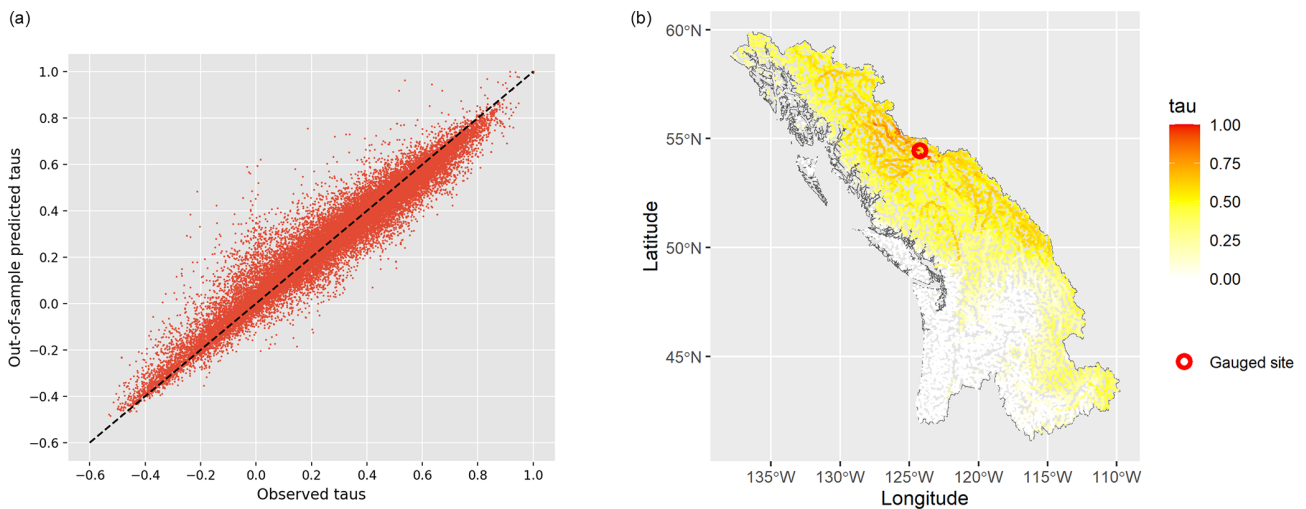


**Figure 7.** Validation of the XGBoost  $\tau$  interpolation model. Out-of-sample Kendall's  $\tau$  predictions are compared with the true values for all pairs of gauge stations (a) using 10-fold cross-validation. Predicted values with respect to one gauge site are shown (b).

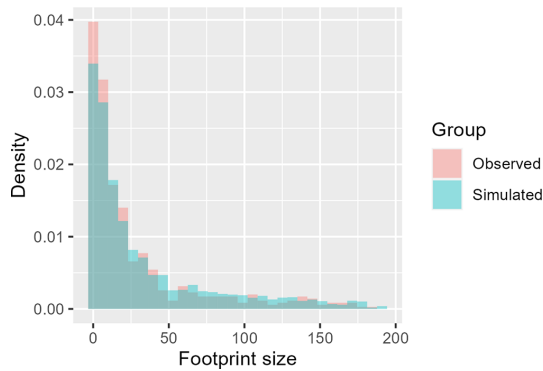


**Figure 8.** Histogram of event footprint sizes, defined as the number of gauges with a flow greater than the 0.9th quantile flow, for observed and simulated events.

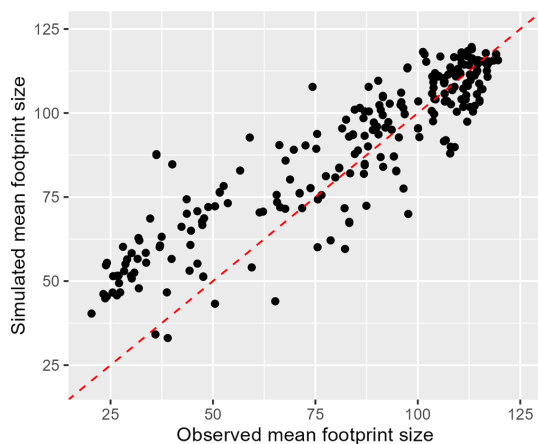


**Figure 9.** Mean event footprint size for the observed and simulated events at each gauge station. The means are calculated over all events impacting each gauge with a flow greater than the 0.9th quantile flow. The dotted red line is the diagonal 1 : 1 line.

extreme flow magnitudes. For the simulated events, return period levels cannot be calculated from annual maxima because some synthetic years have the maximum flow lower than the 0 quantile on the GEV scale, so the actual maximum flows for those years are not known. Instead, for each gauge station the exceedances over the 0.99th quantile threshold (on the event scale) are back-transformed to discharge values using the marginal model in Sect. 4.3.2. They are then used to fit a generalized Pareto distribution and derive the corresponding return period levels. Figure 11 shows that the return period flows calculated from the simulated events slightly underestimate the 20- and 100-year floods. Globally, the flows calculated from the simulated events are very close to the return period flows indicated by the marginal model in Sect. 4.3.2.

## 6 Results

Events from the simulated event set are first inspected visually by plotting maps of some event footprints. In this section, the footprint of an event is defined as the number of catchments experiencing a flow greater than the 5-year return period flow. This will allow easier back-to-back comparisons with results from Quinn et al. (2019). Figure 12 shows four simulated events, chosen to cover a variety of spatial patterns contained in the observed records. The red dots represent all catchments experiencing a flow greater than the 1 in 5-year flow during a given event. Simulated events are diverse in location, footprint size, and pattern. Each event is composed of clearly visible spatial clusters, suggesting that the strong spatial dependence of nearby extreme flows is well captured by the model.

Next, similarly to Quinn et al. (2019), we try to assess the link between event peak magnitude and footprint size. We expect that higher-magnitude floods also present a larger footprint, as this is the conclusion drawn from the Quinn et al. (2019) study of river floods in the US. For any event, its peak magnitude and epicenter are defined as the maximum flow experienced during that event and the location of that flow. Then for a given catchment, the mean event footprint size is defined as the mean footprint size of all events where that catchment is the epicenter. The mean modeled footprint size is spatially represented in Fig. 13 for all catchments, where we have partitioned the events into four categories according to their peak magnitudes. These are greater than 5, 5 to 20, 20 to 100, and greater than 100-year return period ranges, representing all events, high-frequency events, medium-frequency events, and low-frequency events. This analysis is meant to reproduce Fig. 9 in Quinn et al. (2019) to further validate the coherence of our simulated events against a reference paper in spatial flood modeling, except that here we calculate and show the mean event footprint size (in number of catchments) instead of the mean impacted area (in km<sup>2</sup>). The plots show a positive correlation between event peak magnitude and footprint size. Higher-magnitude events typically have a larger spatial footprint, though some spatial variability in this relationship does exist. For example, locations closer to the coastline (west side of the region) present a relatively low mean footprint size, which increases less with event magnitude than inland locations. This might be partly explained by the geography of the coastline composed of many little islands and river networks, which restricts widespread flooding.

Finally, still following Quinn et al. (2019), we look at the distribution of flow magnitudes within each simulated event. To that end, the proportion

$$\pi = \frac{\text{number of catchments with flow} > \text{half the return period of event magnitude}}{\text{number of catchments impacted by the event (flow with return period} > 5 \text{ years)}}$$

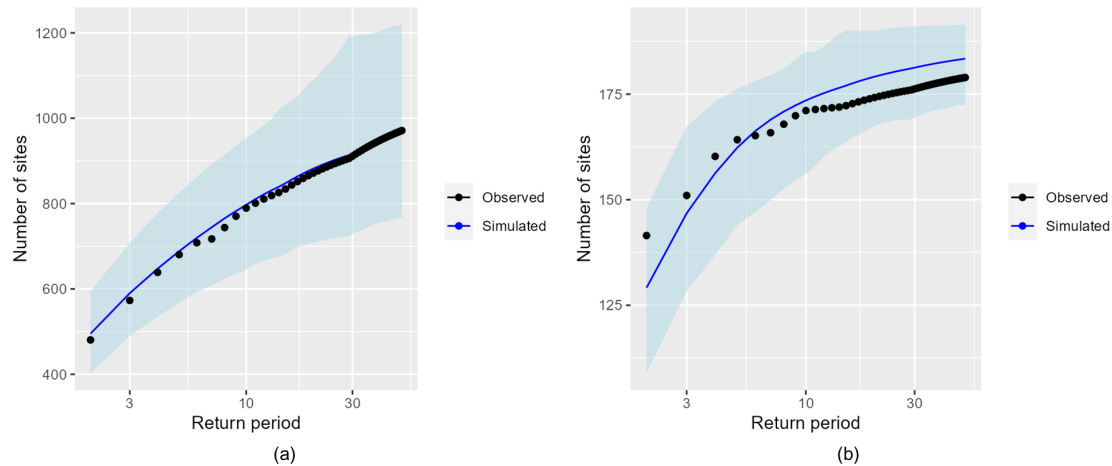


**Figure 10.** Annual loss exceedance curves calculated with the observed (black dots) and simulated (blue line) event sets for the annual aggregate loss (a) and annual maximum loss (b). The 95 % confidence intervals for the simulated loss are included (blue ribbon). They are calculated from 10 000 random 30-year samples from the simulated years.

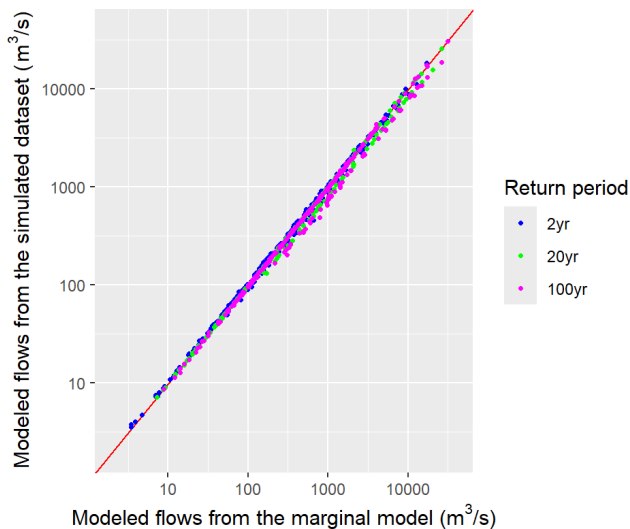


**Figure 11.** Discharge levels with return period 2 (blue), 20 (green), and 100 years (magenta) for all gauge stations, estimated from the synthetic event set and compared with the same quantities derived from the marginal model in Sect. 4.3.2. The red line indicates the 1 : 1 fit.

is calculated for each event. This is the proportion of catchments in a given event with a flow return period higher than the flow corresponding to half the maximum flow return period (RP). For example, for an event with a peak magnitude of 1 in 20-year flow, this proportion is equal to the number of catchments with at least 1 in 10-year flows divided by the number of catchments with at least 1 in 5-year flows. This is meant to represent the proportion of the event footprint which is relatively large. To distinguish the effect of event magnitude, histograms of the proportion of catchments with relatively large flows (as defined above) are plotted, where

events are again divided into four categories of magnitude: greater than 5, 5 to 20, 20 to 100, and greater than 100-year return period (Fig. 14). For floods in the 5- to 20-year return period range, notice the peak at  $\pi = 1$ . This corresponds to all events with peak magnitude lower than the 1 in 10-year flow (by definition, all catchments impacted by such an event experience a magnitude greater than the 1 in 5-year flow). The plots show that as event peak magnitude increases, the proportion of the event footprint which is relatively large decreases. The mean value of this proportion is 19 % for all events, 48 % for 5–20-year return period events, 7.4 % for 20–100-year return period events, and 2 % for > 100-year return period events. This means that for high-magnitude events, despite their widespread behavior (large event footprint size as shown in Fig. 13), significant flooding is concentrated in a small region within the event footprint (low proportion of the event footprint experiencing equivalently extreme flows). This finding agrees with the conclusions from Quinn et al. (2019).

## 7 Discussion

### 7.1 Data

The model we develop for flood spatial dependence is a statistical model which draws information from observed discharge records to simulate synthetic flood events. Station data do not have homogeneous coverage over North America, with sparse gauge density in northern Canadian territories and California. However, most areas with fewer stations are also less populated, which mitigates the negative effects of model underperformance there. Preprocessing and the creation of the synchronous regional datasets impose further temporal constraints which restrict the amount of avail-

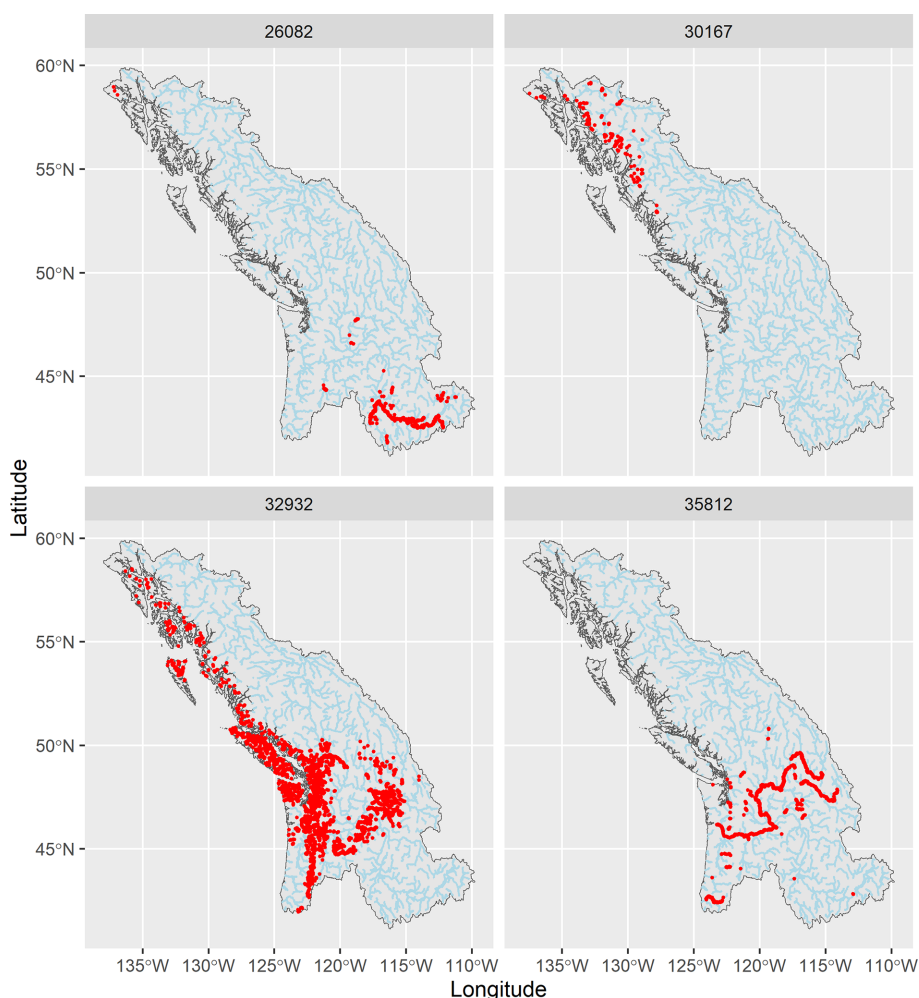


**Figure 12.** Examples of simulated events and their footprints. Red dots are catchments impacted by an event with a flow greater than the 1 in 5-year flow.

able data used to fit the dependence model. Any statistical model is only as good as the quality and quantity of information contained in the data used for estimation. We are fully aware of these limitations and propose some ideas for future work to make use of the most high-quality data available. First, the station gauge data can be supplemented with recently developed remote sensing or radar data, although this would require more extensive preprocessing to put the available sources at the same temporal and spatial resolutions. For some regions, finding a sufficiently long common time period with decent spatial coverage is not possible due to gauge sites having different times of operation. A less stringent condition could be used to subset the data when creating the synchronous discharge set, and possible missing values can be filled using any reasonable gap-filling algorithm, although this kind of procedure can smooth out extreme events and induce additional uncertainty in the model. Finally, hydrological model outputs can be used to augment the observed discharge records, as in Olcese et al. (2022) and Wing

et al. (2020), although this would also introduce uncertainties linked to parameterizing the hydrological model. Additional efforts would also be needed to select suitable input data to the hydrological model and downscale the output discharge.

## 7.2 Dependence model

The Fisher copula used to model the spatial dependence assumes that discharge pairwise Kendall's  $\tau$  coefficients are positive. This is mostly the case in our analysis, although when the considered region is vast and gauge sites are far away, some Kendall's  $\tau$  might be negative. This drawback can theoretically be corrected by replacing the negative values with zero, although this artificial correction induces a distortion in the entries of the correlation matrix  $\Sigma$  after Kendall's  $\tau$  inversion. A possible alternative to alleviate this difficulty is to define clusters of stations within a large region and apply the Fisher copula independently to each cluster, though this would impose strict limits on the event footprints,

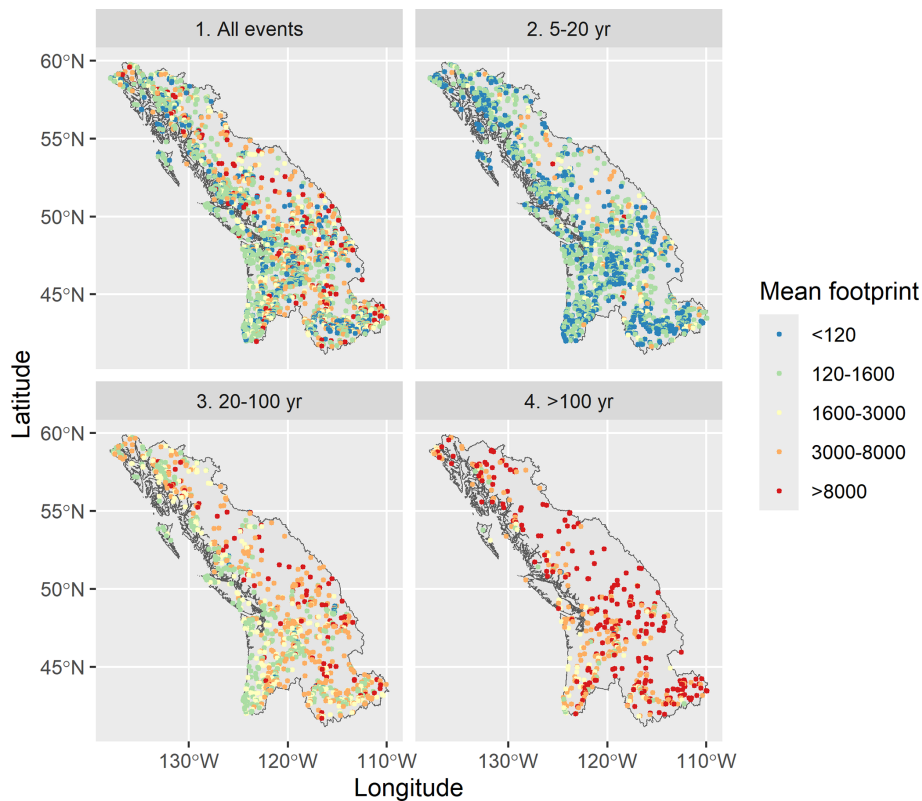


**Figure 13.** Mean event footprint size for catchments experiencing events with peak magnitude within one of four categories ( $> 5$  (all events), 5–20, 20–100, and  $> 100$ -year magnitudes). Each point corresponds to a catchment which is the epicenter of at least one event.

which might be unrealistic. Since the effect on the  $\Sigma$  matrix induced by the negative Kendall's  $\tau$  is not overwhelming for our data, we did not pursue further modeling efforts to explicitly account for negative Kendall's  $\tau$ .

The marginal modeling approach we follow is quite unconventional. Usually in a multivariate setting with copulas, the variables are transformed to and back-transformed from the uniform scale using the same fitted distributions. We instead make the choice to back-transform the simulated values using a marginal model operating on the annual scale, which fits GEV distributions to annual maxima. This choice is mainly motivated by the better quality and quantity of annual maximum discharge data at our disposal compared to the regional event set. For example, the regional event set for region 9 spans 30 years and covers a subset of 253 gauge sites. In contrast, for this region, high-quality annual maxima data are available for more than 2000 stations, with records spanning 34 years on average. Dense gauge coverage over the region brings much needed information to better predict extreme flows at ungauged catchments. Back-transforming values using a marginal model on the annual scale requires transforming the simulated values from the event scale to the annual scale, a step which is validated in Sect. 5.3. The adopted approach does not allow recovering discharge values lower than the lower bound of the GEV distributions (quan-

tile 0 on the annual scale), but this is not a nuisance since we are interested in the extreme discharges only.

Using XGBoost to interpolate the Kendall's  $\tau$  to ungauged catchments presents major advantages and improvement upon previous methods used in the literature to model spatial patterns for ungauged locations. A machine learning model like XGBoost draws its strength from the relatively high amount of information contained in the 130 covariates and the pairwise Kendall's  $\tau$ . Furthermore, using a decision-tree-based model allows capturing possibly nonlinear patterns in the spatial structure of discharge. Finally, compared to more parameterized models like neural networks, boosting models like XGBoost are much faster to train and yield satisfying results.

The novel conditional simulation strategy for ungauged catchments is particularly suited to our data thanks to its computational efficiency. The British Columbia region is divided into 98 980 catchments. The alternative of simulating values at all catchments at once would entail calculating a full correlation matrix of size  $98\,980 \times 98\,980$ . This is a huge computational challenge in terms of both memory storage and calculation time, as such a matrix is not sparse and inverting it is virtually impossible. Moreover, in order to derive the full matrix, Kendall's  $\tau$  between all pairs of ungauged catchments would need to be predicted. Those can be

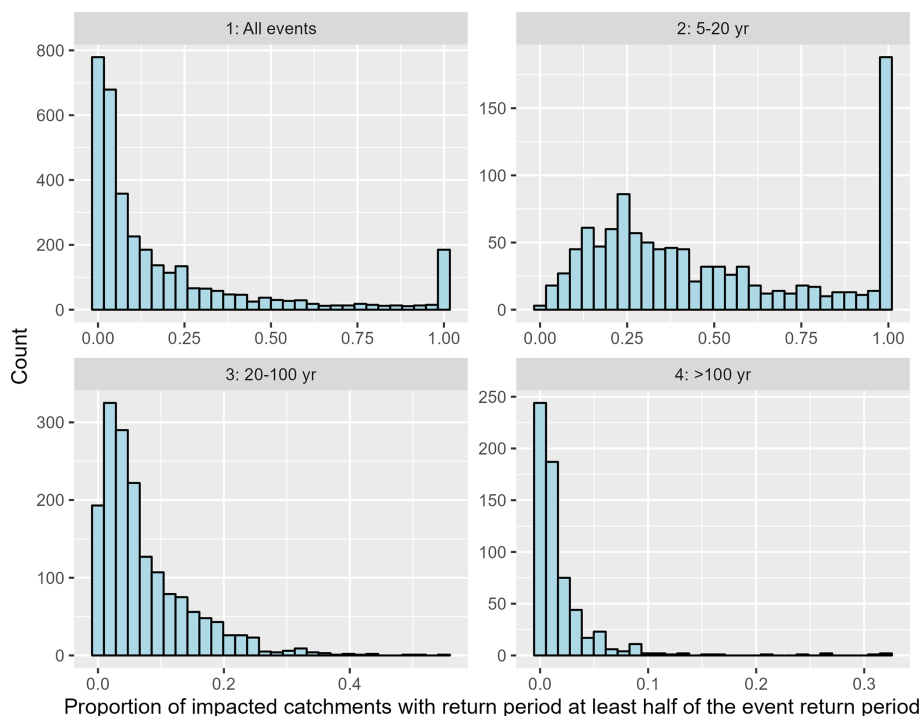


**Figure 14.** Histograms of the proportion of catchments in a given event with flow return period at least half the maximum event flow return period. The events are divided into four categories of magnitude: greater than 5, 5 to 20, 20 to 100, and greater than 100-year return period ranges.

harder to estimate, especially for pairs of catchments which are geographically distant from any gauge site. Finally, extending the correlation matrix to include all ungauged catchments would possibly alter the optimal degree of freedom  $\nu$  of the Fisher copula, as the matrix size would be multiplied by the order of hundreds. In contrast, conditional simulation of each ungauged catchment changes the correlation matrix by only one column and row. Brunner et al. (2019) showed that the degree of freedom parameter of the Fisher copula is only weakly sensitive to an extension of the correlation matrix. Thus, since we only add one row and column, it is reasonable to assume that the estimated  $\nu$  stays at the same value. In summary, the conditional simulation strategy bypasses many complications which can arise if all simulated events were computed simultaneously. It avoids the prediction of Kendall's  $\tau$  between ungauged catchments, the inversion of a huge correlation matrix, and the recalculation of the degree of freedom  $\nu$ . The dependence model developed for ungauged catchments is thus computationally very efficient. When parallelized on 20 cores, 50 000 simulated events for all catchments in region 9 can be computed in under half an hour.

## 8 Conclusions

This study introduces a novel methodology to model spatial dependence between riverine floods with application to North America based on the Fisher copula (Favre et al., 2018; Brunner et al., 2019). The model developed in Brunner et al. (2019) is modified to be applicable to a much larger spatial scale and number of gauge sites. In particular, the Kendall's  $\tau$  interpolation model uses a machine learning approach to draw strength from the 130 catchment attributes, and a conditional simulation strategy is devised to simulate flood values efficiently, without computing the full correlation matrix. Using this model, a synthetic event set of arbitrary size can be simulated, with characteristics resembling the observed events and a more accurate sampling of the most extreme events. As this study aims to highlight the novelty of the introduced methodology and its validation, for results we focus our attention on the general picture drawn in the simulated events rather than possible local details. We find that similar general conclusions as in Quinn et al. (2019) can be drawn with regard to flood spatial dependence, namely the following.

- Riverine floods usually occur in spatial clusters, reflecting the strong connectivity of river networks.
- Higher-magnitude flood events tend to have a higher event footprint.

- Despite being widespread, higher-magnitude flood events tend to have the most extreme magnitudes concentrated around a small area.

The spatially coherent event set can be integrated in a hydraulic model and flood loss model to calculate flood depth, damage to buildings, and financial losses for each simulated event. Because spatial dependence is explicitly modeled, we expect that losses calculated from the event catalog are more reliable. Overall, the methodology presented in this study provides a valuable tool for stakeholders (governments, municipalities, insurance and reinsurance companies) to better understand and manage flood risk, contributing to enhancing society's global resilience to flood disasters.

**Data availability.** The gauge data used in the paper are available online in the GRDC database (<https://grdc.bafg.de/>, The Global Runoff Data Centre, 2024), on the USGS website (<https://waterdata.usgs.gov/nwis>, U.S. Geological Survey, 2016), and on dedicated Canadian and Quebec platforms (<https://collaboration.cmc.ec.gc.ca/cmc/hydrometrics/www/>, Environment Canada, 2013 and <https://www.cehq.gouv.qc.ca/atlas-hydroclimatique/index.htm>, Ministère de l'Environnement, de la Lutte contre les changements climatiques, de la Faune et des Parcs, 2022). The catchment covariates are compiled from data sources available online. The output event set and model data layers are proprietary of Geosapiens Inc. in nature but can be made available for research use only. For further inquiries regarding access to our data and code, please contact Geosapiens Inc. directly.

**Supplement.** The supplement related to this article is available online at: <https://doi.org/10.5194/hess-28-5069-2024-supplement>.

**Author contributions.** The methodology, coding, statistical analysis, result validation, and manuscript writing were undertaken by DAA. Guidance, manuscript reviewing, and some coding were undertaken by CC. Catchment delineation procedures and some manuscript writing were undertaken by JG-F. All authors have read and agreed to the published version of the manuscript.

**Competing interests.** The contact author has declared that none of the authors has any competing interests.

**Disclaimer.** Publisher's note: Copernicus Publications remains neutral with regard to jurisdictional claims made in the text, published maps, institutional affiliations, or any other geographical representation in this paper. While Copernicus Publications makes every effort to include appropriate place names, the final responsibility lies with the authors.

**Acknowledgements.** We would like to thank fellow Geosapiens team members Mingke Erin Li and Amit Kumar for their help with

downloading and providing information on datasets used. We also thank former team member Fan Zhang for her help in the delineation of the HydroBASINS regions.

**Financial support.** This research has been supported by the Investissement Québec (Innovation Program), with grant no. 61118.

**Review statement.** This paper was edited by Yue-Ping Xu and reviewed by two anonymous referees.

## References

- Alaya, M. A. B., Zwiers, F., and Zhang, X.: Probable Maximum Precipitation: Its Estimation and Uncertainty Quantification Using Bivariate Extreme Value Analysis, *J. Hydrometeorol.*, 19, 679–694, <https://doi.org/10.1175/JHM-D-17-0110.1>, 2018.
- Allen, G. H., David, C. H., Andreadis, K. M., Hossain, F., and Famiglietti, J. S.: Global Estimates of River Flow Wave Travel Times and Implications for Low-Latency Satellite Data, *Geophys. Res. Lett.*, 45, 7551–7560, <https://doi.org/10.1029/2018GL077914>, 2018.
- Bates, P. D., Quinn, N., Sampson, C., Smith, A., Wing, O., Sosa, J., Savage, J., Olcese, G., Neal, J., Schumann, G., Giustarini, L., Coxon, G., Porter, J. R., Amodeo, M. F., Chu, Z., Lewis-Gruss, S., Freeman, N. B., Houser, T., Delgado, M., Hamidi, A., Bolliger, I., E. McCusker, K., Emanuel, K., Ferreira, C. M., Khalid, A., Haigh, I. D., Couasnon, A., E. Kopp, R., Hsiang, S., and Krajewski, W. F.: Combined Modeling of US Fluvial, Pluvial, and Coastal Flood Hazard Under Current and Future Climates, *Water Resour. Res.*, 57, e2020WR028673, <https://doi.org/10.1029/2020WR028673>, 2021.
- Bates, P. D., Savage, J., Wing, O., Quinn, N., Sampson, C., Neal, J., and Smith, A.: A climate-conditioned catastrophe risk model for UK flooding, *Nat. Hazards Earth Syst. Sci.*, 23, 891–908, <https://doi.org/10.5194/nhess-23-891-2023>, 2023.
- Berghuijs, W. R., Allen, S. T., Harrigan, S., and Kirchner, J. W.: Growing Spatial Scales of Synchronous River Flooding in Europe, *Geophys. Res. Lett.*, 46, 1423–1428, <https://doi.org/10.1029/2018GL081883>, 2019.
- Brunner, M. I., Furrer, R., and Favre, A.-C.: Modeling the spatial dependence of floods using the Fisher copula, *Hydrol. Earth Syst. Sci.*, 23, 107–124, <https://doi.org/10.5194/hess-23-107-2019>, 2019.
- Brunner, M. I., Gilleland, E., Wood, A., Swain, D. L., and Clark, M.: Spatial Dependence of Floods Shaped by Spatiotemporal Variations in Meteorological and Land-Surface Processes, *Geophys. Res. Lett.*, 47, e2020GL088000, <https://doi.org/10.1029/2020GL088000>, 2020.
- Centre for Research on the Epidemiology of Disasters: The Human Cost of Natural Disasters – A global perspective, [https://www.cred.be/sites/default/files/The\\_Human\\_Cost\\_of\\_Natural\\_Disasters\\_CRED.pdf](https://www.cred.be/sites/default/files/The_Human_Cost_of_Natural_Disasters_CRED.pdf) (last access: 14 November 2024), 2015.
- Coles, S., Bawa, J., Trenner, L., and Dorazio, P.: An introduction to statistical modeling of extreme values, vol. 208, Springer, ISBN 10 1849968748, ISBN 13 978-1849968744, 2001.



- Comaniciu, D. and Meer, P.: Mean shift: a robust approach toward feature space analysis, *IEEE T. Pattern Anal.*, 24, 603–619, <https://doi.org/10.1109/34.1000236>, 2002.
- Cooley, D., Naveau, P., and Poncet, P.: *Variograms for spatial max-stable random fields*, 373–390, Springer New York, New York, NY, [https://doi.org/10.1007/0-387-36062-X\\_17](https://doi.org/10.1007/0-387-36062-X_17), 2006.
- Davison, A. C., Padoan, S. A., and Ribatet, M.: *Statistical Modeling of Spatial Extremes*, *Stat. Sci.*, 27, 161–186, <https://doi.org/10.1214/11-STS376>, 2012.
- de Haan, L. and Ferreira, A.: *Extreme Value Theory: An Introduction*, Springer, New York, ISBN 10 0387344713, ISBN 13 9780387344713, 2006.
- Diederer, D., Liu, Y., Gouldby, B., Diermanse, F., and Vorogushyn, S.: Stochastic generation of spatially coherent river discharge peaks for continental event-based flood risk assessment, *Nat. Hazards Earth Syst. Sci.*, 19, 1041–1053, <https://doi.org/10.5194/nhess-19-1041-2019>, 2019.
- Environment Canada: HYDAT Database – Canada, Environment Canada [data set], <https://collaboration.cmc.ec.gc.ca/cmc/hydrometrics/www/> (last access: 10 November 2024), 2013.
- Favre, A.-C., Quessy, J.-F., and Toupin, M.-H.: The new family of Fisher copulas to model upper tail dependence and radial asymmetry: Properties and application to high-dimensional rainfall data, *Environmetrics*, 29, e2494, <https://doi.org/10.1002/env.2494>, 2018.
- Genest, C. and Favre, A.-C.: Everything You Always Wanted to Know about Copula Modeling but Were Afraid to Ask, *J. Hydrol. Eng.*, 12, 347–368, 2007.
- Grinsztajn, L., Oyallon, E., and Varoquaux, G.: Why do tree-based models still outperform deep learning on typical tabular data?, in: *Proceedings of the 36th International Conference on Neural Information Processing Systems, NIPS '22*, Curran Associates Inc., Red Hook, NY, USA, ISBN 9781713871088, 2024.
- Gräler, B.: Modelling skewed spatial random fields through the spatial vine copula, *Spat. Stat.*, 10, 87–102, <https://doi.org/10.1016/j.spasta.2014.01.001>, 2014.
- Hastie, T., Tibshirani, R., and Friedman, J.: *The Elements of Statistical Learning*, Springer, ISBN 10 0387848843, ISBN 13 9780387848846, 2009.
- Heffernan, J. E. and Tawn, J. A.: A Conditional Approach for Multivariate Extreme Values (with Discussion), *J. R. Stat. Soc. B*, 66, 497–546, <https://doi.org/10.1111/j.1467-9868.2004.02050.x>, 2004.
- Higham, N. J.: Computing the nearest correlation matrix – a problem from finance, *IMA J. Numer. Anal.*, 22, 329–343, <https://doi.org/10.1093/imanum/22.3.329>, 2002.
- Keef, C., Svensson, C., and Tawn, J. A.: Spatial dependence in extreme river flows and precipitation for Great Britain, *J. Hydrol.*, 378, 240–252, <https://doi.org/10.1016/j.jhydrol.2009.09.026>, 2009.
- Keef, C., Tawn, J. A., and Lamb, R.: Estimating the probability of widespread flood events, *Environmetrics*, 24, 13–21, <https://doi.org/10.1002/env.2190>, 2013.
- Lee, D. and Joe, H.: Multivariate extreme value copulas with factor and tree dependence structures, *Extremes (Boston)*, 21, 147–176, <https://doi.org/10.1007/s10687-017-0298-0>, 2018.
- Lehner, B. and Grill, G.: Global river hydrography and network routing: baseline data and new approaches to study the world's large river systems, *Hydrol. Process.*, 27, 2171–2186, <https://doi.org/10.1002/hyp.9740>, 2013.
- Ministère de l'Environnement, de la Lutte contre les changements climatiques, de la Faune et des Parcs: Atlas hydroclimatique, Ministère de l'Environnement, de la Lutte contre les changements climatiques, de la Faune et des Parcs [data set], <https://www.cehq.gouv.qc.ca/atlas-hydroclimatique/index.htm> (last access: 10 November 2024), 2022.
- Neal, J., Keef, C., Bates, P., Beven, K., and Leedal, D.: Probabilistic flood risk mapping including spatial dependence, *Hydrol. Process.*, 27, 1349–1363, <https://doi.org/10.1002/hyp.9572>, 2013.
- Nearing, G. S., Kratzert, F., Sampson, A. K., Pelissier, C. S., Klotz, D., Frame, J. M., Prieto, C., and Gupta, H. V.: What Role Does Hydrological Science Play in the Age of Machine Learning?, *Water Resour. Res.*, 57, e2020WR028091, <https://doi.org/10.1029/2020WR028091>, 2021.
- Olcese, G., Bates, P. D., Neal, J. C., Sampson, C. C., Wing, O. E. J., Quinn, N., and Beck, H. E.: Use of Hydrological Models in Global Stochastic Flood Modeling, *Water Resour. Res.*, 58, e2022WR032743, <https://doi.org/10.1029/2022WR032743>, 2022.
- Quinn, N., Bates, P. D., Neal, J., Smith, A., Wing, O., Sampson, C., Smith, J., and Heffernan, J.: The Spatial Dependence of Flood Hazard and Risk in the United States, *Water Resour. Res.*, 55, 1890–1911, <https://doi.org/10.1029/2018WR024205>, 2019.
- Ribatet, M. and Sedki, M.: Extreme value copulas and max-stable processes, *Journal de la société française de statistique*, 154, 138–150, 2013.
- Rougier, J. C.: Quantifying Natural Hazard Risk, in: *Risk and Uncertainty Assessment for Natural Hazards*, edited by: Rougier, J. C., Sparks, R. S. J., and Hill, L. J., 19–39, Cambridge University Press, UK, <https://doi.org/10.1017/CBO9781139047562.003>, 2013.
- Schmid, F. and Schmidt, R.: Multivariate extensions of Spearman's rho and related statistics, *Stat. Probabil. Lett.*, 77, 407–416, <https://doi.org/10.1016/j.spl.2006.08.007>, 2007.
- Schulte, M. and Schumann, A. H.: Extensive spatio-temporal assessment of flood events by application of pair-copulas, *P. Int. Ass. Hydrol. Sci.*, 370, 177–181, 2015.
- Serinaldi, F., Bárdossy, A., and Kilsby, C. G.: Upper tail dependence in rainfall extremes: would we know it if we saw it?, *Stoch. Evn. Res. Risk A.*, 29, 1211–1233, <https://doi.org/10.1007/s00477-014-0946-8>, 2015.
- The Global Runoff Data Centre: <https://grdc.bafg.de/>, last access: 10 November 2024.
- U.S. Geological Survey: National Water Information System data available on the World Wide Web (USGS Water Data for the Nation), <https://waterdata.usgs.gov/nwis> (last access: 10 November 2024), 2016.
- Wing, O. E. J., Quinn, N., Bates, P. D., Neal, J. C., Smith, A. M., Sampson, C. C., Coxon, G., Yamazaki, D., Sutanudjaja, E. H., and Alfieri, L.: Toward Global Stochastic River Flood Modeling, *Water Resour. Res.*, 56, e2020WR027692, <https://doi.org/10.1029/2020WR027692>, 2020.
- Yamazaki, D., Ikeshima, D., Sosa, J., Bates, P. D., Allen, G. H., and Pavelsky, T. M.: MERIT Hydro: A High-Resolution Global Hydrography Map Based on Latest Topography Dataset, *Water Resour. Res.*, 55, 5053–5073, <https://doi.org/10.1029/2019WR024873>, 2019.